Dual-Energy Low-keV or Single-Energy Low-kV CT for Endoleak Detection?: A 6-Reader Study in an Aortic Aneurysm Phantom

Skawran, Stephan ; Angst, Florian ; Blüthgen, Christian ; Eberhard, Matthias ; Kälin, Pascal ; Kobe, Adrian ; Nagy, Daniel ; Szucs-Farkas, Zsolt ; Alkadhi, Hatem ; Euler, André

Abstract: OBJECTIVES: The aim of this study was to compare image quality, conspicuity, and endoleak detection between single-energy low-kV images (SEIs) and dual-energy low-keV virtual monoenergetic images (VMIs+) in computed tomography angiography of the aorta after endovascular repair. MATERIALS AND METHODS: An abdominal aortic aneurysm phantom simulating 36 endoleaks (2 densities; diameters: 2, 4, and 6 mm) in a medium- and large-sized patient was used. Each size was scanned using single-energy at 80 kVp (A) and 100 kVp (B), and dual-energy at 80/Sn150kVp for the medium (C) and 90/Sn150kVp for the large size (D). VMIs+ at 40 keV and 50 keV were reconstructed from protocols C and D. Radiation dose was 3 mGy for the medium and 6 mGy for the large size. Objective image quality and normalized noise power spectrum were determined. Subjective image quality, conspicuity, and sensitivity for endoleaks were independently assessed by 6 radiologists. Sensitivity was compared using Marascuilo procedure and Fisher exact test. Conspicuities were compared using Wilcoxon-matched pairs test, analysis of variance, and Tukey test. RESULTS: The contrast-to-noise-ratio of the aorta was significantly higher for VMI+ compared with SEI ($P < 0.001$). Noise power spectrum showed a higher noise magnitude and coarser texture in VMI+. Subjective image quality and overall conspicuity was lower for VMI+ compared with SEI ($P < 0.05$). Sensitivity for endoleaks was overall higher in the medium phantom for SEI (60.9% for A, 62.2% for B) compared with VMI+ (54.2% for C, 49.3% for D) with significant differences between protocols B and D ($P < 0.05$). In the large phantom, there was no significant difference in sensitivity among protocols ($P = 0.79$), with highest rates for protocols B (31.4%) and C (31.7%). CONCLUSIONS: Our study indicates that low-keV VMI+ results in improved contrast-to-noise-ratio of the aorta, whereas noise properties, subjective image quality, conspicuity, and sensitivity for endoleaks were overall superior for SEI.

DOI: https://doi.org/10.1097/RLI.0000000000000606

Dual-Energy Low-keV or Single-Energy Low-kV CT for Endoleak Detection?

A 6-Reader Study in an Aortic Aneurysm Phantom

Stephan Skawran, MD, Florian Angst, MD,* Christian Blüthgen, MD, MS,* Matthias Eberhard, MD, EBCR,* Pascal Kälin, MD,* Adrian Kobe, MD,* Daniel Nagy, MD,* Zsolt Szucs-Farkas, MD,† Hatem Alkadhi, MD, MPH, EBCR, FESER,* and André Euler, MD**

Objectives: The aim of this study was to compare image quality, conspicuity, and endoleak detection between single-energy low-kV images (SEIs) and dual-energy low-keV virtual monoenergetic images (VMIs+) in computed tomography angiography of the aorta after endovascular repair.

Materials and Methods: An abdominal aortic aneurysm phantom simulating 36 endoleaks (2 densities; diameters: 2, 4, and 6 mm) in a medium- and large-sized patient was used. Each size was scanned using single-energy at 80 kVp (A) and 100 kVp (B), and dual-energy at 80/Sn150kVp for the medium (C) and 90/Sn150kVp for the large size (D). VMIs+ at 40 keV and 50 keV were reconstructed from protocols C and D. Radiation dose was 3 mGy for the medium and 6 mGy for the large size. Objective image quality and normalized noise power spectrum were determined. Subjective image quality, conspicuity, and sensitivity for endoleaks were independently assessed by 6 radiologists. Sensitivity was compared using Marascuilo procedure and Fisher exact test. Conspicuities were compared using Wilcoxon-matched pairs test, analysis of variance, and Tukey test.

Results: The contrast-to-noise-ratio of the aorta was significantly higher for VMI+ compared with SEI ($P < 0.001$). Noise power spectrum showed a higher noise magnitude and coarser texture in VMI+. Subjective image quality and overall conspicuity was lower for VMI+ compared with SEI ($P < 0.05$). Sensitivity for endoleaks was overall higher in the medium phantom for SEI (60.9% for A, 62.2% for B) compared with VMI+ (54.2% for C, 49.3% for D) with significant differences between protocols B and D ($P < 0.05$). In the large phantom, there was no significant difference in sensitivity among protocols ($P = 0.79$), with highest rates for protocols B (31.4%) and C (31.7%).

Conclusions: Our study indicates that low-keV VMI+ results in improved contrast-to-noise-ratio of the aorta, whereas noise properties, subjective image quality, conspicuity, and sensitivity for endoleaks were overall superior for SEI.

Key Words: multidetector computed tomography, aortic aneurysm, abdominal, endovascular procedures, endoleak, phantoms, imaging

(*Invest Radiol* 2019;00: 00–00)

Endovascular aortic repair (EVAR) of aneurysms has been established as an alternative to open surgery with similar rates of long-term survival.[1] Endoleak in the aneurysmal sac, which occurs in approximately 26% of patients after EVAR, is the most common complication and can lead to aneurysm rupture.[2,3] Patients have to undergo life-long follow-up imaging to rule out peri-interventional and postinterventional complications.[4] Different imaging modalities, for example, computed tomography (CT), contrast-enhanced ultrasound (CEUS), or magnetic resonance imaging, are available for follow-up,[2] and because of the necessity for repetitive imaging, surveillance radiation dose considerations have become a focus of interest.

Multiphase single-energy CT angiography of the aorta (CTA) represents the current criterion standard for imaging surveillance of patients after EVAR. It typically consists of a multiphase acquisition including a noncontrast, arterial, and delayed phase of enhancement.[5] Some recent studies suggested the use of low tube voltages for single-energy CTA (low-kV SEI)[6] because low-kV SEI increases the CT attenuation and contrast-to-noise ratio (CNR) in structures containing iodine[7] and is associated with less radiation dose.[8,9]

With the introduction of dual-energy CT (DECT), further alternatives to improve iodine attenuation and to decrease radiation dose have become clinically available. Here, second-generation virtual monoenergetic images (VMIs+) reconstructed from DECT improve the CNR of iodine at low-keV levels by combining the high signal at lower energies with the noise properties at medium energies.[10–16] This has shown potential also for CTA.[17,18] Notably, no study so far has directly compared which of the 2 different techniques, that is, low-kV SEI and VMI+, performs better in dedicated CTA applications.

Thus, the purpose of our study was to compare objective and subjective image quality, normalized noise power spectrum (nNPS), conspicuity, and sensitivity for endoleaks between low-kV SEI and low-keV VMI+ for CTA after EVAR.

MATERIALS AND METHODS

Phantom Design

A custom-made aortic phantom (Endoleak Phantom; QRM, Moehrendorf, Germany) was used in this study. The phantom consisted of a cylinder made of epoxy resin (21 cm in *z*-axis), simulating an aneurysmal sac. A fillable hole covered with a metal stent graft (Valiant; Medtronic, Dublin, Ireland) was located centrally within this cylinder, simulating the perfused aortic lumen after endovascular repair (diameter 2 cm). Multiple discs made of resin and organic iodine were distributed along the *z*-axis of the cylinder to simulate a total of 36 endoleaks (diameters of 2, 4, and 6 mm). These endoleaks were positioned at an axial distance of 0, 5, or 10 mm from the metal stent graft. Half of the endoleaks measured a CT attenuation of 130 HU, whereas the other half measured 180 HU at 100 kVp. The phantom was mounted along the central longitudinal axis of 2 separate, water-filled, cylindrical containers with different diameters (30 and 40 cm), simulating the abdominal cross-sections of a medium-sized (estimated body weight, 72–85 kg) and large-sized (estimated body weight, 118–142 kg) patient (Fig. 1). The central hole of the phantom was filled with a 1:37 dilution of iodinated contrast medium (iopromide) at a concentration of 370 mg/mL (Ultravist 370; Bayer AG, Leverkusen, Germany) and water to reach an attenuation of approximately 290 HU at 100 kVp.

Received for publication May 29, 2019; and accepted for publication, after revision, July 6, 2019.

From the *Institute for Diagnostic and Interventional Radiology, University Hospital Zurich, University of Zurich, Zurich; and †Institute of Radiology, Hospital Centre of Biel, Biel, Switzerland.

Conflicts of interest and sources of funding: none declared.

Correspondence to: Hatem Alkadhi, MD, MPH, EBCR, FESER, Institute for Diagnostic and Interventional Radiology, University Hospital Zurich, Rämistrasse 100, 8091 Zurich, Switzerland. E-mail: hatem.alkadhi@usz.ch.

ISSN: 0020-9996/19/0000–0000
DOI: 10.1097/RLI.0000000000000606

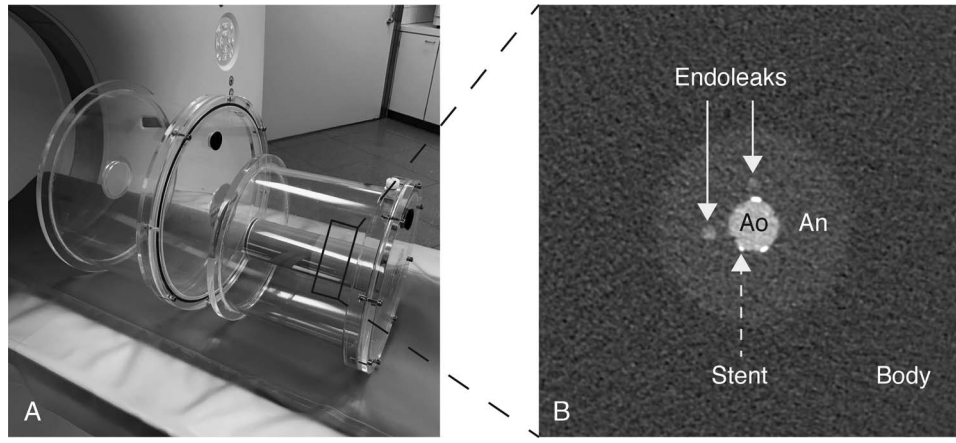

FIGURE 1. A, Image of the 2 water containers emulating a large and medium patient with the abdominal aortic aneurysm endoleak phantom cylinder placed in the medium container. B, Transverse CT image of the phantom cylinder at 100 kVp with the central iodine-filled lumen, simulating the perfused stent-lumen in the aorta (Ao) surrounded by a metal mesh graft (dashed arrow). The aneurysm (An) contains two 4-mm endoleaks (arrows) at 2 and 4 mm distance from the stent (arrows). The cylinder is embedded in a water-filled container (body).

Computed Tomography Protocols and Data Reconstruction

The phantom was repeatedly imaged in helical mode on a 192-slice dual-source CT scanner (SOMATOM Force; Siemens Healthineers, Forchheim, Germany). The reference tube current time product (ref. mAs) was adjusted before each scan to reach an estimated volume CT dose index ($CTDI_{vol}$) of 3 mGy for the medium and 6 mGy for the large phantom. These values were chosen to reflect typical radiation dose levels encountered in individual phases of a CTA after EVAR at our institution. Computed tomography scans were repeated 4 times for each scan condition. For each scan, axial images with a slice thickness of 2 mm and increment of 1.6 mm were reconstructed. Advanced modeled iterative reconstruction at a strength-level of 3 and a Qr40-kernel was used. The following scans and corresponding reconstructions were applied:

A. Single-energy CT at 80 kVp
   a. Medium phantom: $CTDI_{vol}$, 3 mGy; ref. mAs, 156 mAs
   b. Large phantom: $CTDI_{vol}$, 6 mGy; ref. mAs, 313 mAs

B. Single-energy CT at 100 kVp
   a. Medium phantom: $CTDI_{vol}$, 3 mGy; ref. mAs, 75 mAs
   b. Large phantom: $CTDI_{vol}$, 6 mGy; ref. mAs, 150 mAs

C. Dual-energy CT at 80/Sn150kVp in the medium phantom
   $CTDI_{vol}$, 3 mGy; ref. mAs, 89 mAs (tube A)/45 mAs (tube B)
   VMI+ reconstructions at 40 keV and at 50 keV

D. Dual-energy CT at 90/Sn150 kVp in the large phantom
   $CTDI_{vol}$, 3 mGy; ref. mAs, 120 mAs (tube A)/75 mAs (tube B)
   VMI+ reconstructions at 40 keV and at 50 keV

VMIs+ were reconstructed[10] on a vendor-specific software platform (VMI+, Syngo.via VB30A; Siemens Healthineers).

Postprocessing

To avoid recall bias between the 4 repeats of each of the 4 reconstruction groups, we changed the orientation and distribution of the endoleaks. Each reconstructed dataset was cut into 3 equally sized axial image stacks using an open-source software (Horos; Horosproject.org, Annapolis, MD). These image stacks were flipped, rotated by 90 degrees in *x*-*y* plane, permutated in a randomized fashion, and merged to obtain a single CT stack containing a total of 504 axial images. These merged datasets were made available for interpretation on our hospital's picture archiving and communication system (IMPAX; Agfa Healthcare, Mortsel, Belgium).

Assessment of Objective Image Quality

Computed tomography attenuation was measured in all phantom components. Regions of interest (ROIs) were placed in the aortic lumen, the aneurysmal sac, in one high and one low attenuating 6-mm endoleak, and in the water within the surrounding containers. Noise was defined as the standard deviation of attenuation of the water. Contrast-to-noise ratios were calculated for the aorta as CNR_{aorta} = [Att (aorta) − Att (aneurysm)]/Noise, for which Att (*x*) was the mean CT attenuation value in the organ *x*. Contrast-to-noise ratio of the endoleaks was calculated as $CNR_{endoleak}$ = [Att (endoleak) − Att (aneurysm)]/Noise. Measurements were performed 3 times for each of the 4 repetitions of each reconstruction group (12 overall measurements for 1 group).

Assessment of Noise Power Spectrum

The nNPS was assessed to characterize both the noise magnitude and texture for all 4 groups of reconstructions. According to a standardized method,[19–21] four 32 × 32 square ROIs were placed in the uniform water surrounding the aneurysm. One hundred ten slices were used for each nNPS calculation (4 ROIs per slice × 110 = 440 ROIs). An open-source software package was used (imQuest; Duke University, Durham, NC). Average (F_{av}) and peak spatial frequency (F_{peak}) were used to compare noise texture among reconstructions. Finer noise texture was described by higher F_{peak} values, whereas lower F_{peak} values indicated coarser texture.

Assessment of Subjective Image Quality, Conspicuity, and Sensitivity for Endoleaks

For each phantom size, 3 radiologists independently assessed the 4 different reconstruction groups for the presence of endoleaks. Reader experience was matched between the 2 reader groups. There was 1 board-certified radiologist (expert reader) and 2 radiology residents in each group (group 1: with 6, 3, 3; group 2: 9, 3, 2 years of experience in radiology, respectively). We chose 2 different groups of readers to further reduce recall bias of endoleak location. Readers were blinded to the endoleak features (number, size, density, location) as well as to the scan and reconstruction parameters. Each reader had to mark the position using a circular ROI and grade the conspicuity of each detected endoleak. Readers were given a pictorial manual to grade the conspicuity of detected endoleaks using a 3-point scale (1, possible endoleak; 2, probable endoleak; 3, definite endoleak). Readers were allowed to

scroll, zoom, and adjust the window width and level. The readout was performed in a fixed order starting with VMI+ 40 keV, followed by VMI+ 50 keV, 80 kVp, and 100 kVp, as this specific order seemed to reflect decreasing difficulty for endoleak detection after preliminary review. After review, the readers were asked to rate overall image quality for each group on a 5-point scale (5, very good; 4, good; 3, intermediate; 2, poor; 1, very poor quality). The reader's conspicuity, image quality ratings, and marked endoleak positions were saved into a picture archiving and communication system and reviewed by one radiologist using the construction plan.

Statistical Analysis

Marks made by the readers were compared with the construction plan of the phantom and classified as true-positive or false-positive. Missed lesions were regarded as false-negative. Readers' data were averaged for statistical analysis. Sensitivity and mean conspicuity for different sizes and densities of endoleaks with each CT protocol were calculated. Sensitivities were compared using Marascuilo procedure for comparing multiple proportions and Fisher exact test as appropriate. Mean conspicuities were compared using Wilcoxon-matched pairs test, analysis of variance, and Tukey test. Kendall coefficient of concordance was calculated to estimate interreader variability. Analyses were performed using the Statistica software package (Version 7; Statsoft, Tulsa, OK) and a Web-based calculator (http://www.obg.cuhk.edu.hk/ResearchSupport/StatTools/MultiProps_Pgm.php). The level of statistical significance was set at $P < 0.05$.

RESULTS

Objective Image Quality

Detailed results are summarized in Table 1. The CT attenuation and CNR of the aorta were significantly higher in VMI+ compared with SEI for both phantom sizes (all $P < 0.001$). Both parameters increased with decreasing tube voltage and keV level. Overall, CNR of the endoleaks was lower in VMI+ compared with SEI. This difference was statistically significant for the less-dense endoleak in the medium phantom ($P < 0.001$).

Image noise was significantly higher in VMI+ compared with SEI for both phantom sizes (all $P < 0.001$). Noise increased with phantom size, decreasing tube voltage, and decreasing keV level.

Noise Power Spectrum

Noise texture differed among the 4 reconstruction groups, with a shift toward lower spatial frequencies in VMI+ compared with SEI for both phantom sizes (see Fig. 2, A and B). F_{av} and F_{peak} were lower for VMI+ compared with SEI ($F_{av\text{-}medium}$: 0.19 vs 0.24; $F_{av\text{-}large}$: 0.17 vs 0.21; $F_{peak\text{-}medium}$: 0.06 vs 0.17; $F_{peak\text{-}large}$: 0.06 vs 0.17).

Subjective Image Quality, Conspicuity, and Detection Sensitivity

Detailed results are summarized in Tables 2 and 3 and Figure 3. Overall, subjective image quality was lower for VMI+ compared with SEI (medium, 1.8 vs 4.0; large, 1.5 vs 3.7). Ratings were lowest for VMI+ 40 keV in both phantoms (medium, 1.3; large, 1) and highest for 100 kVp in the medium phantom (4.3).

Conspicuity differed significantly among readers for both phantom sizes (all $P < 0.001$). Here, the Kendall coefficient of concordance was low for both groups (medium phantom, 0.09; large phantom, 0.05). Overall, endoleak conspicuity was significantly higher for SEI compared with VMI+ for the medium phantom ($P < 0.0001$). There was no significant difference between 80 kVp and 100 kVp ($P = 0.26$) as well as between VMI+ 40 and 50 keV ($P = 0.17$). In the large phantom, a significant difference in conspicuity was only found for 100 kVp, which showed significantly higher conspicuity compared with the other 3 reconstruction groups (all $P < 0.05$). A subanalysis by endoleak diameter and density revealed that conspicuity increased significantly with increasing diameter and density for both phantom sizes (all $P < 0.001$).

TABLE 1. Objective Image Quality in the Medium and Large Phantom

	80 kVp (A)		100 kVp (B)		VMI+ 50 keV (C)		VMI+ 40 keV (D)		*P*	
	M	L	M	L	M	L	M	L	M	L
CT attenuation, HU										
Aorta	374 ± 3	400 ± 8	281 ± 4	294 ± 8	546 ± 5	543 ± 8	834 ± 8	830 ± 13	<0.001	<0.002
Aneurysm	40 ± 3	48 ± 2	39 ± 4	42 ± 5	42 ± 4	47 ± 8	43 ± 6	50 ± 14	0.14–1.0	0.12–1.0
Body	0 ± 1	2 ± 2	1 ± 1	2 ± 2	−7 ± 3	3 ± 4	−11 ± 6	6 ± 8	A vs B: 0.97; all others: <0.003	0.23–1
Noise	24 ± 2	45 ± 3	23 ± 2	39 ± 3	28 ± 1	55 ± 3	40 ± 2	79 ± 4	A vs B: 0.89; all others: <0.001	<0.001
Endoleak 1	174 ± 8	177 ± 25	159 ± 12	165 ± 20	201 ± 19	197 ± 28	254 ± 35	265 ± 45	A vs B: 0.30; all others: <0.001	D vs A, B, C: <0.001; all others: <0.06
Endoleak 2	127 ± 6	132 ± 13	121 ± 8	126 ± 19	125 ± 11	143 ± 36	146 ± 21	183 ± 46	D vs A, B, C: <0.006; all others: 0.65–0.97	D vs A, B, C: <0.001; all others: 0.53–0.97
CNR										
Aorta	16.0 ± 1.0	8.9 ± 0.6	12.3 ± 1.3	7.6 ± 0.7	19.5 ± 0.8	9.9 ± 0.6	21.4 ± 1.0	10.5 ± 0.6	<0.001	C vs D, 0.11; all others: <0.001
Endoleak 1	5.7 ± 0.3	2.9 ± 0.6	5.3 ± 0.7	3.2 ± 0.6	5.6 ± 0.6	2.7 ± 0.5	5.3 ± 0.9	2.7 ± 0.6	0.31–0.99	0.22–0.6
Endoleak 2	3.7 ± 0.4	1.9 ± 0.3	3.6 ± 0.3	2.2 ± 0.6	2.9 ± 0.3	1.8 ± 0.7	2.6 ± 0.4	1.7 ± 0.6	A vs B: 0.70; C vs D: 0.09; all others: <0.001	0.17–0.99

Measurements of CT attenuation in Hounsfield Units (HU) for the various phantom components and contrast-to-noise ratios of the iodine containing parts given as means ± standard deviation.

M indicates medium; L, large; CT, computed tomography; CNR, contrast-to-noise ratio.

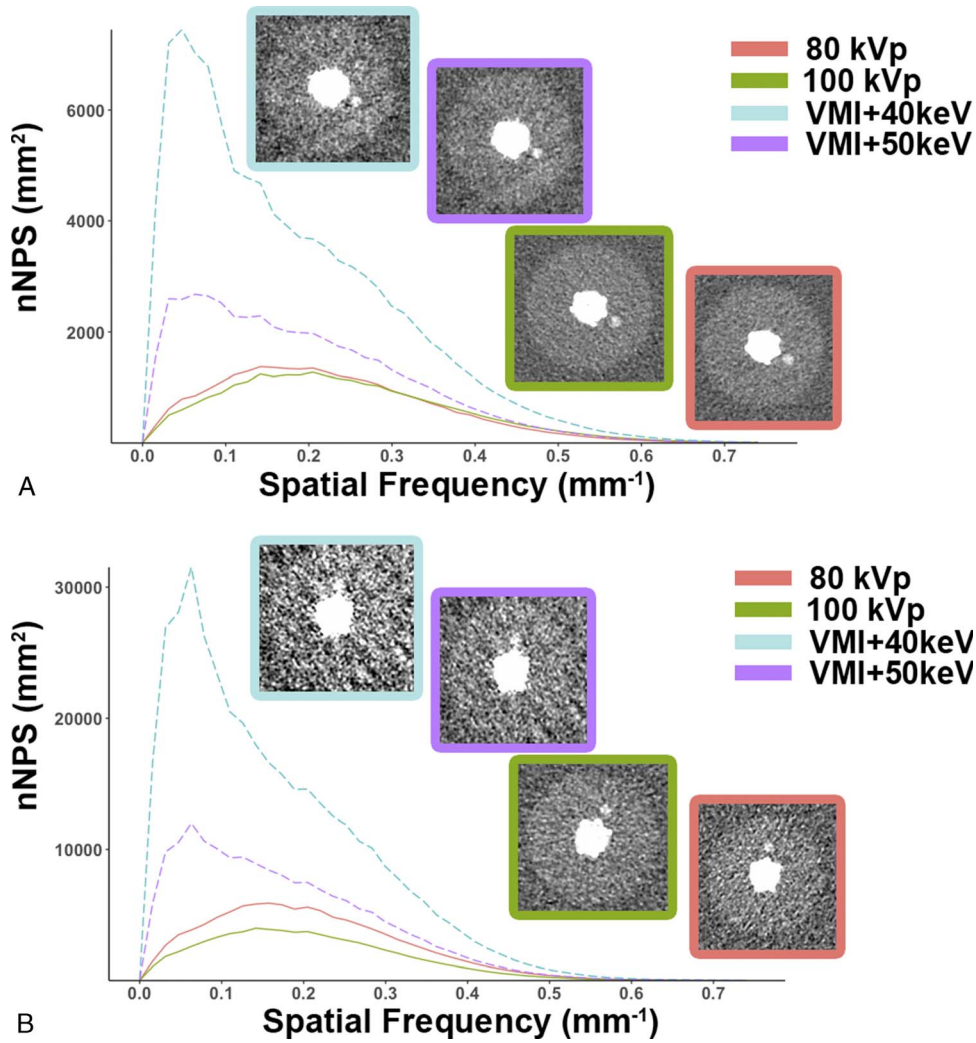

FIGURE 2. Graphs and axial CT images show normalized noise power spectrum (nNPS) and noise texture for SEI at 80 kVp (red), SEI at 100 kVp (green), VMI+ 50 keV (purple), and VMI+ 40 keV (light blue) for the medium (A) and large phantom (B). Lower frequencies are present in VMI+ compared with SEI. This difference in frequency distributions contributes to the differences in noise texture as depicted in the axial slices.

Sensitivity of endoleak detection was significantly lower for reader 3 compared with both other readers for the medium phantom ($P < 0.05$). There was no significant difference among the 3 readers for the large phantom ($P = 0.143$). Overall sensitivity was 60.9%, 62.2%, 54.2%, and 49.3% for 80 kVp, 100 kVp, VMI+ 40 keV, and VMI+ 50 keV, respectively, for the medium size, and 28%, 31.4%, 31.7%, and 28% for 80 kVp, 100 kVp, VMI+ 40 keV, and VMI+ 50 keV, respectively, for the large size. For the medium phantom, overall sensitivity was significantly lower for VMI+ 40 keV (49.3%) compared with 100 kVp (62.2%) ($P = 0.032$; see Fig. 3). For the large phantom, there was no significant difference among the 4 groups ($P = 0.79$). Sensitivity decreased with increasing phantom size (on average, 56.7% and 29.8% for the medium and large phantom, respectively).

A subanalysis by endoleak diameter revealed that sensitivity was significantly affected by diameter for both phantom sizes (all $P < 0.0001$). Overall, sensitivity was high to intermediate for the 6-mm diameter (on average, 97.9% for the medium and 68.8% for the large phantom), intermediate to low for the 4-mm diameter (on average, 70.5% for the medium and 19.8% for the large phantom), and very low for the 2-mm diameter (on average, 1.6% for the medium and 0.9% for the large phantom). There was no significant difference among the 4 reconstruction groups for the 6-mm and 2-mm endoleaks for both phantom sizes ($P = 0.1–1$) nor for the 4-mm endoleaks in the large phantom ($P = 0.69$). However, the sensitivity for the detection of 4-mm endoleaks was significantly lower for VMI+ compared with SEI for the medium phantom (all $P < 0.05$). A subanalysis by endoleak density revealed that sensitivity increased significantly with increasing density for both phantom sizes (both $P < 0.05$). There was no significant difference among the 4 reconstruction groups ($P = 0.2–0.9$).

DISCUSSION

Our comparison between low-keV VMI+ and low-kV SEI in CTA for endoleak detection after EVAR revealed improved CNR of the aorta for low-keV VMI+ and superior noise properties, subjective image quality, conspicuity, and overall improved endoleak detection for low-kV SEI.

Based on prior studies, which reported an improvement in quantitative image quality by low-keV VMI+,[10–16,22–24] we aimed to assess if this beneficial effect could be exploited to improve endoleak detection. Increased iodine attenuation of low-keV VMI+ is based on the fact that their energy levels (40 and 50 keV) are closer to the k-edge of

TABLE 2. Conspicuity and Subjective Image Quality for the Medium Phantom

Parameter	80 kVp (A)	100 kVp (B)	VMI+ 50 keV (C)	VMI+ 40 keV (D)	*P*
Mean conspicuity rating/mean image quality rating					
All	2.11/3.7	2.23/4.3	1.81/2.3	1.67/1.3	A vs C, D: <0.0001 B vs C, D: <0.0001 All others: 0.18–0.26
Diameter 1	0.33	0.67	0.56	0.33	All $P = 1$
Diameter 2	1.53	1.69	1.15	0.97	A vs C: <0.05 A vs D: <0.0001 B vs C, D: <0.0001 All others: 0.83–0.89
Diameter 3	2.74	2.83	2.43	2.33	A vs C: <0.05 A vs D: <0.001 B vs C: <0.001 B vs D: <0.0001 All others: 1.0
Density 1	1.77	1.93	1.44	1.27	A vs D: <0.0001 A vs C: <0.05 All others: 0.66
Density 2	2.44	2.54	2.19	2.07	A vs D: <0.01 All others: 0.18–0.92

Data shows overall subjective image quality for each group, overall mean conspicuity ratings, and subanalyses for the 3 different endoleak diameters and 2 endoleak densities.

iodine (33.2 keV) compared with SEI at 80 kVp (mean energy of 44 keV) and 100 kVp (mean energy of 52 keV).

To date, only a few studies have assessed the impact of VMI+ on diagnostic accuracy in vascular imaging.[4,25–27] However, these studies compared VMI+ with conventional or blended images at 120 kVp. Our study adds to the literature by comparing the diagnostic impact of VMI+ to low-kV SEI. Martin et al[25] found a significantly higher endoleak detection rate using VMI+ 40 keV compared with first-generation VMI and to standard linearly blended images. In that study,[25] diagnostic accuracy was based on scoring the level of confidence for the presence or absence of an endoleak. In contrast, our study compared VMI+ to the current reference standard for vascular CTA, that is, low-kV SEI, and we asked readers to mark the presence and location of endoleaks.

We found improved sensitivity for endoleaks for SEI compared with VMI+ in the medium phantom. In the large phantom, however, sensitivity was highest for 100 kVp and VMI+ 50 keV. We attribute the lower sensitivity of 80 kVp and VMI+ 40 keV to the increased photon absorption of low-energy photons in the large phantom, leading to increased image noise. Notably, the overall sensitivity for endoleaks was substantially lower in our study (up to 62.2% in the medium and 31.7% in the large phantom, respectively) compared with the reported sensitivity in the literature (83%).[28] A subanalysis of the 6-mm endoleaks, however, demonstrated high sensitivity in the medium phantom (97.9%) and an intermediate sensitivity in the large phantom (68.8%). Therefore, we attribute this difference to the overall very low detection rate of the 2-mm and 4-mm endoleaks. Still, it must be acknowledged that the impact of endoleaks less than 6 mm on patient management is still controversial and there are currently no size-based guidelines for reintervention.

We found significantly higher attenuation and CNR of the aorta and higher attenuation of the endoleaks in VMI+ compared with SEI. However, due to the significantly increased image noise in VMI+ compared with SEI, the CNR of the endoleaks was slightly lower in VMI+. Although former studies have reported only a slight increase in image noise using VMI+ 40 keV,[29] we observed a significant increase when decreasing the energy level from 50 keV to 40 keV at low radiation dose

TABLE 3. Conspicuity and Subjective Image Quality for the Large Phantom

Parameter	80 kVp (A)	100 kVp (B)	VMI+ 50 keV (C)	VMI+ 40 keV (D)	*P*
Mean conspicuity rating/mean image quality rating					
All	1.19/4	1.57/3.3	1.20/2	1.15/1	A vs D: <0.0001 All others: 0.98–0.99
Diameter 1	0.33	—	—	0.50	—
Diameter 2	0.75	0.93	0.84	0.89	1.0
Diameter 3	1.42	1.78	1.38	1.28	A vs D: <0.0001 All others: 0.8–0.99
Density 1	0.81	1.13	0.94	0.91	0.77–1.0
Density 2	1.34	1.87	1.32	1.28	B vs A: <0.01 B vs C: <0.05 B vs D: <0.001 All others: 1.0

Data shows overall subjective image quality for each group, overall mean conspicuity ratings, and subanalyses for the 3 different endoleak diameters and 2 endoleak densities.

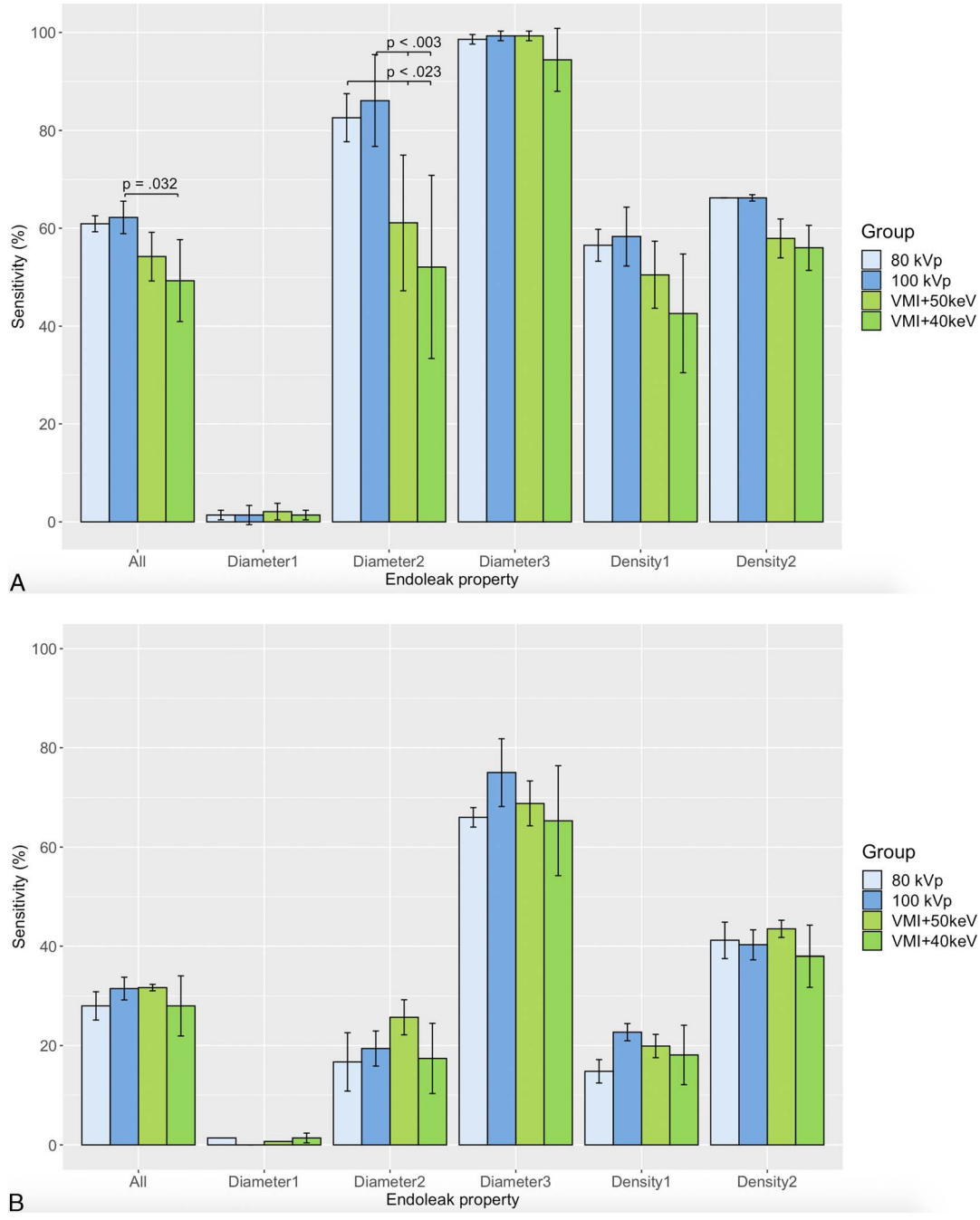

FIGURE 3. Barplots show sensitivity for endoleaks overall and subdivided by endoleak property. Data are presented as mean sensitivity with standard deviation for the 4 groups for the medium (A) and large (B) phantom. Significant comparisons are indicated. Note significant differences in overall sensitivity between 100 kVp and VMI+ 40 keV in the medium phantom.

levels. In addition to standard noise measurements, we assessed the noise texture of VMI+ and SEI using the nNPS and found substantial differences in the shape of the nNPS between VMI+ and SEI. In VMI+, the spectrum was shifted toward lower spatial frequencies, indicating coarser and "blotchier" noise texture.[30] This shift parallels the changes observed for iterative reconstruction algorithms compared with filtered back projection.[21] Differences in noise texture may alter radiologists' perception of image quality and may potentially affect the sensitivity of lesion detection. We hypothesize that these potential differences in the readers' perception are reflected by the poor interobserver agreement for lesion conspicuity found for both reader groups.

Our results highlight that an improvement in objective image quality, such as attenuation or CNR, must not necessarily correlate with improved diagnostic accuracy. Former studies indicated that CNR is not task-specific and shows no significant correlation with human performance for the detection of low-contrast lesions.[31–33] Consequently, every novel imaging technology should be scrutinized by its impact on diagnostic accuracy for a particular clinical task in an observer study. However, these observer studies are labor-intensive, time-consuming,

and impractical considering the various potential clinical tasks and scan parameters. First attempts to improve this association between image quality and accuracy in a standardized and automated fashion have been made with the proposal of a detectability index.[34]

The following limitations of our study merit consideration. First, our phantom had a cylindrical shape and did not include additional anatomic structures such as bone or parenchymal organs. Second, endoleaks were investigated in a nondynamic single phase and were limited to a fixed number of diameters and CT attenuation features. Third, 2 different reader groups assessed the detection accuracy for the medium and large phantom. However, we purposely chose this study design to decrease recall bias of the readers. Fourth, the tube voltage settings of DECT differed between the medium (80/Sn150kVp) and large phantom (90/Sn150kVp). We purposely chose a higher tube voltage setting in the large phantom based on prior research, which has shown that the use of 80 kVp negatively impacted DECT-based iodine quantification in large phantoms due to increased image noise. Fifth, we did not perform a comparison to other imaging modalities such as CEUS or magnetic resonance imaging. Sixth, the phantom did not include slices without endoleaks, and it was therefore not possible to determine true-negative findings for calculating the specificity. However, a high sensitivity is important in endoleak detection considering the increased rate of missed endoleaks found in CTA compared with CEUS and considering the potential impact on patient treatment. Seventh, we limited our investigation to a single radiation dose level per phantom, and we intentionally chose a low radiation dose protocol that is typically used in our routine clinical practice. We might assume that results may differ at other, higher radiation dose levels. Finally, we did not assess DECT-based virtual noncontrast images,[35] which could be used to replace a separate noncontrast scan, thus further reducing the radiation dose to the patient.

In conclusion, our ex vivo study results advocate the use of low-kV SEI for endoleak detection in patients with EVAR, with SEI at 100 kVp demonstrating overall highest sensitivity for both phantom sizes.

ACKNOWLEDGMENTS

The authors thank Mrs Sarah Scuiletti for revising the manuscript.

REFERENCES

1. Bulder RMA, Bastiaannet E, Hamming JF, et al. Meta-analysis of long-term survival after elective endovascular or open repair of abdominal aortic aneurysm. *Br J Surg*. 2019;106:523–533.
2. Cassagnes L, Perignon R, Amokrane F, et al. Aortic stent-grafts: endoleak surveillance. *Diagn Interv Imaging*. 2016;97:19–27.
3. Guo Q, Zhao J, Huang B, et al. A systematic review of ultrasound or magnetic resonance imaging compared with computed tomography for endoleak detection and aneurysm diameter measurement after endovascular aneurysm repair. *J Endovasc Ther*. 2016;23:936–943.
4. Javor D, Wressnegger A, Unterhumer S, et al. Endoleak detection using single-acquisition split-bolus dual-energy computer tomography (DECT). *Eur Radiol*. 2017;27:1622–1630.
5. Partovi S, Trischman T, Rafailidis V, et al. Multimodality imaging assessment of endoleaks post-endovascular aortic repair. *Br J Radiol*. 2018;91:20180013.
6. Ippolito D, Talei Franzesi C, Fior D, et al. Low kV settings CT angiography (CTA) with low dose contrast medium volume protocol in the assessment of thoracic and abdominal aorta disease: a feasibility study. *Br J Radiol*. 2015;88:20140140.
7. Martens B, Hendriks BMF, Eijsvoogel NG, et al. Individually body weight-adapted contrast media application in computed tomography imaging of the liver at 90 kVp. *Invest Radiol*. 2019;54:177–182.
8. Leithner D, Wichmann JL, Mahmoudi S, et al. Diagnostic yield of 90-kVp low-tube-voltage carotid and intracerebral CT-angiography: effects on radiation dose, image quality and diagnostic performance for the detection of carotid stenosis. *Br J Radiol*. 2018;91:20170927.
9. Higashigaito K, Schmid T, Puippe G, et al. CT angiography of the aorta: prospective evaluation of individualized low-volume contrast media protocols. *Radiology*. 2016;280:960–968.
10. Grant KL, Flohr TG, Krauss B, et al. Assessment of an advanced image-based technique to calculate virtual monoenergetic computed tomographic images from a dual-energy examination to improve contrast-to-noise ratio in examinations using iodinated contrast media. *Invest Radiol*. 2014;49:586–592.
11. Husarik DB, Gordic S, Desbiolles L, et al. Advanced virtual monoenergetic computed tomography of hyperattenuating and hypoattenuating liver lesions: ex-vivo and patient experience in various body sizes. *Invest Radiol*. 2015;50:695–702.
12. Albrecht MH, Trommer J, Wichmann JL, et al. Comprehensive comparison of virtual monoenergetic and linearly blended reconstruction techniques in third-generation dual-source dual-energy computed tomography angiography of the thorax and abdomen. *Invest Radiol*. 2016;51:582–590.
13. Leithner D, Wichmann JL, Vogl TJ, et al. Virtual monoenergetic imaging and iodine perfusion maps improve diagnostic accuracy of dual-energy computed tomography pulmonary angiography with suboptimal contrast attenuation. *Invest Radiol*. 2017;52:659–665.
14. Dane B, Patel H, O'Donnell T, et al. Image quality on dual-energy CTPA virtual monoenergetic images: quantitative and qualitative assessment. *Acad Radiol*. 2018;25:1075–1086.
15. Lenga L, Czwikla R, Wichmann JL, et al. Dual-energy CT in patients with colorectal cancer: improved assessment of hypoattenuating liver metastases using noise-optimized virtual monoenergetic imaging. *Eur J Radiol*. 2018;106:184–191.
16. Beer L, Toepker M, Ba-Ssalamah A, et al. Objective and subjective comparison of virtual monoenergetic vs. polychromatic images in patients with pancreatic ductal adenocarcinoma. *Eur Radiol*. 2019.
17. Meier A, Higashigaito K, Martini K, et al. Dual energy CT pulmonary angiography with 6g iodine–a propensity score-matched study. *PLoS One*. 2016;11:e0167214.
18. Chalian H, Kalisz K, Rassouli N, et al. Utility of virtual monoenergetic images derived from a dual-layer detector-based spectral CT in the assessment of aortic anatomy and pathology: a retrospective case control study. *Clin Imaging*. 2018;52:292–301.
19. Solomon JB, Christianson O, Samei E. Quantitative comparison of noise texture across CT scanners from different manufacturers. *Med Phys*. 2012;39:6048–6055.
20. Solomon J, Wilson J, Samei E. Characteristic image quality of a third generation dual-source MDCT scanner: noise, resolution, and detectability. *Med Phys*. 2015;42:4941–4953.
21. Euler A, Solomon J, Marin D, et al. A third-generation adaptive statistical iterative reconstruction technique: phantom study of image noise, spatial resolution, lesion detectability, and dose reduction potential. *AJR Am J Roentgenol*. 2018;210:1301–1308.
22. Ghandour A, Sher A, Rassouli N, et al. Evaluation of virtual monoenergetic images on pulmonary vasculature using the dual-layer detector-based spectral computed tomography. *J Comput Assist Tomogr*. 2018;42:858–865.
23. Neuhaus V, Grosse Hokamp N, Abdullayev N, et al. Comparison of virtual monoenergetic and polyenergetic images reconstructed from dual-layer detector CT angiography of the head and neck. *Eur Radiol*. 2018;28:1102–1110.
24. Nagayama Y, Iyama A, Oda S, et al. Dual-layer dual-energy computed tomography for the assessment of hypovascular hepatic metastases: impact of closing k-edge on image quality and lesion detectability. *Eur Radiol*. 2019;29:2837–2847.
25. Martin SS, Wichmann JL, Weyer H, et al. Endoleaks after endovascular aortic aneurysm repair: improved detection with noise-optimized virtual monoenergetic dual-energy CT. *Eur J Radiol*. 2017;94:125–132.
26. Weiss J, Notohamiprodjo M, Bongers M, et al. Effect of noise-optimized monoenergetic postprocessing on diagnostic accuracy for detecting incidental pulmonary embolism in portal-venous phase dual-energy computed tomography. *Invest Radiol*. 2017;52:142–147.
27. Leithner D, Mahmoudi S, Wichmann JL, et al. Evaluation of virtual monoenergetic imaging algorithms for dual-energy carotid and intracerebral CT angiography: effects on image quality, artefacts and diagnostic performance for the detection of stenosis. *Eur J Radiol*. 2018;99:111–117.
28. Harky A, Zywicka E, Santoro G, et al. Is contrast-enhanced ultrasound (CEUS) superior to computed tomography angiography (CTA) in detection of endoleaks in post-EVAR patients? A systematic review and meta-analysis. *J Ultrasound*. 2019;22:65–75.
29. Meier A, Wurnig M, Desbiolles L, et al. Advanced virtual monoenergetic images: improving the contrast of dual-energy CT pulmonary angiography. *Clin Radiol*. 2015;70:1244–1251.
30. Kwon H, Cho J, Oh J, et al. The adaptive statistical iterative reconstruction-V technique for radiation dose reduction in abdominal CT: comparison with the adaptive statistical iterative reconstruction technique. *Br J Radiol*. 2015;88:20150463.

31. Schindera ST, Odedra D, Raza SA, et al. Iterative reconstruction algorithm for CT: can radiation dose be decreased while low-contrast detectability is preserved? *Radiology*. 2013;269:511–518.
32. Solomon J, Samei E. Correlation between human detection accuracy and observer model-based image quality metrics in computed tomography. *J Med Imaging (Bellingham)*. 2016;3:035506.
33. Euler A, Stieltjes B, Szucs-Farkas Z, et al. Impact of model-based iterative reconstruction on low-contrast lesion detection and image quality in abdominal CT: a 12-reader-based comparative phantom study with filtered back projection at different tube voltages. *Eur Radiol*. 2017;27:5252–5259.
34. Smith TB, Solomon J, Samei E. Estimating detectability index in vivo: development and validation of an automated methodology. *J Med Imaging (Bellingham)*. 2018;5:031403.
35. Obmann MM, Kelsch V, Cosentino A, et al. Interscanner and intrascanner comparison of virtual unenhanced attenuation values derived from twin beam dual-energy and dual-source, dual-energy computed tomography. *Invest Radiol*. 2019;54:1–6.